Research Article | Vol. 6, No. 11 | 1 Nov 2016 | OPTICAL MATERIALS EXPRESS 3651

Optical Materials EXPRESS

Improved efficiency of perovskite solar cells based on Ni-doped ZnO nanorod arrays and Li salt-doped P3HT layer for charge collection

PIN-YAO CHEN AND SHENG-HSIUNG YANG*

Institute of Lighting and Energy Photonics, National Chiao Tung University, 301, Gaofa 3rd Road, Guiren Dist., Tainan 71150, Taiwan
yangsh@mail.nctu.edu.tw

Abstract: We demonstrate regular-type perovskite solar cells based on vertically grown Ni-doped ZnO nanorod arrays and doped P3HT for solar energy harvesting. PCBM was introduced between Ni-doped ZnO nanorod arrays and the perovskite layer to improve electron extraction, while P3HT doped with bis(trifluoromethane)sulfonimide lithium salt (Li-TFSI) was used as hole transporting layer. Three types of perovskite materials, including $MAPbI_3$, $(MA)_x(FA)_{1-x}PbI_3$, and $(MA)_y(GA)_{1-y}PbI_3$, were used as light harvesting layers to exploit conversion efficiency of photovoltaic devices. The optimized perovskite solar cell with the configuration of ITO/Ni-doped ZnO nanorods/PCBM/$(MA)_y(GA)_{1-y}PbI_3$/P3HT + Li-TFSI/Au revealed an open-circuit voltage of 0.83 V, a short-circuit current density of 23.73 mA/cm^2, a fill factor of 70%, and a power conversion efficiency of 13.79%.

OCIS codes: (160.4236) Nanomaterials; (220.4241) Nanostructure fabrication; (040.5350) Photovoltaic; (350.6050) Solar energy.

References and links

1. A. Kojima, K. Teshima, Y. Shirai, and T. Miyasaka, "Organometal halide perovskites as visible-light sensitizers for photovoltaic cells," J. Am. Chem. Soc. **131**(17), 6050–6051 (2009).
2. H.-S. Kim, C.-R. Lee, J.-H. Im, K.-B. Lee, T. Moehl, A. Marchioro, S.-J. Moon, R. Humphry-Baker, J.-H. Yum, J. E. Moser, M. Grätzel, and N.-G. Park, "Lead iodide perovskite sensitized all-solid-state submicron thin film mesoscopic solar cell with efficiency exceeding 9%," Sci. Rep. **2**, 591 (2012).
3. Z. Xiao, C. Bi, Y. Shao, Q. Dong, Q. Wang, Y. Yuan, C. Wang, Y. Gao, and J. Huang, "Efficient, high yield perovskite photovoltaic devices grown by interdiffusion of solution-processed precursor stacking layers," Energy Environ. Sci. **7**(8), 2619–2623 (2014).
4. J. Burschka, N. Pellet, S.-J. Moon, R. Humphry-Baker, P. Gao, M. K. Nazeeruddin, and M. Grätzel, "Sequential deposition as a route to high-performance perovskite-sensitized solar cells," Nature **499**(7458), 316–319 (2013).
5. W. S. Yang, J. H. Noh, N. J. Jeon, Y. C. Kim, S. Ryu, J. Seo, and S. I. Seok, "High-performance photovoltaic perovskite layers fabricated through intramolecular exchange," Science **348**(6240), 1234–1237 (2015).
6. B.-S. Jeong, D. P. Norton, and J. D. Budai, "Conductivity in transparent anatase TiO_2 films epitaxially grown by reactive sputtering deposition," Solid-State Electron. **47**(12), 2275–2278 (2003).
7. A. Tsukazaki, A. Ohtomo, and M. Kawasaki, "High-mobility electronic transport in ZnO thin films," Appl. Phys. Lett. **88**(15), 152106 (2006).
8. C. S. Ponseca, Jr., T. J. Savenije, M. Abdellah, K. Zheng, A. Yartsev, T. Pascher, T. Harlang, P. Chabera, T. Pullerits, A. Stepanov, J.-P. Wolf, and V. Sundström, "Organometal halide perovskite solar cell materials rationalized: ultrafast charge generation, high and microsecond-long balanced mobilities, and slow recombination," J. Am. Chem. Soc. **136**(14), 5189–5192 (2014).
9. Z. Zang, X. Zeng, J. Du, M. Wang, and X. Tang, "Femtosecond laser direct writing of microholes on roughened ZnO for output power enhancement of InGaN light-emitting diodes," Opt. Lett. **41**(15), 3463–3466 (2016).
10. Z. Zang, A. Nakamura, and J. Temmyo, "Single cuprous oxide films synthesized by radical oxidation at low temperature for PV application," Opt. Express **21**(9), 11448–11456 (2013).
11. D. Liu and T. L. Kelly, "Perovskite solar cells with a planar heterojunction structure prepared using room-temperature solution processing techniques," Nat. Photonics **8**(2), 133–138 (2013).
12. J. Song, E. Zheng, X.-F. Wang, W. Tian, and T. Miyasaka, "Low-temperature-processed ZnO–SnO_2 nanocomposite for efficient planar perovskite solar cells," Sol. Energy Mater. Sol. Cells **144**, 623–630 (2016).
13. X. Zhao, H. Shen, Y. Zhang, X. Li, X. Zhao, M. Tai, J. Li, J. Li, X. Li, and H. Lin, "Aluminum-Doped Zinc Oxide as Highly Stable Electron Collection Layer for Perovskite Solar Cells," ACS Appl. Mater. Interfaces **8**(12), 7826–7833 (2016).

#275779 http://dx.doi.org/10.1364/OME.6.003651
Journal © 2016 Received 13 Sep 2016; revised 20 Oct 2016; accepted 20 Oct 2016; published 27 Oct 2016

Optical Materials EXPRESS

14. D.-Y. Son, J.-H. Im, H.-S. Kim, and N.-G. Park, "11% efficient perovskite solar cell based on ZnO nanorods: an effective charge collection system," J. Phys. Chem. C **118**(30), 16567–16573 (2014).
15. J. Dong, Y. Zhao, J. Shi, H. Wei, J. Xiao, X. Xu, J. Luo, J. Xu, D. Li, Y. Luo, and Q. Meng, "Impressive enhancement in the cell performance of ZnO nanorod-based perovskite solar cells with Al-doped ZnO interfacial modification," Chem. Commun. (Camb.) **50**(87), 13381–13384 (2014).
16. K. Mahmood, B. S. Swain, and A. Amassian, "Core-shell heterostructured metal oxide arrays enable superior light-harvesting and hysteresis-free mesoscopic perovskite solar cells," Nanoscale **7**(30), 12812–12819 (2015).
17. K. Mahmood, B. S Swain, and A. Amassian, "Double-layered ZnO nanostructures for efficient perovskite solar cells," Nanoscale **6**(24), 14674–14678 (2014).
18. S. S. Reddy, K. Gunasekar, J. H. Heo, S. H. Im, C. S. Kim, D.-H. Kim, J. H. Moon, J. Y. Lee, M. Song, and S.-H. Jin, "Highly Efficient Organic Hole Transporting Materials for Perovskite and Organic Solar Cells with Long-Term Stability," Adv. Mater. **28**(4), 686–693 (2016).
19. M.-J. Sher, J. A. Bartelt, T. M. Burke, A. Salleo, M. D. McGehee, and A. M. Lindenberg, "Time-and Temperature-Independent Local Carrier Mobility and Effects of Regioregularity in Polymer-Fullerene Organic Semiconductors," Adv. Electron. Mater. **2**(3), 1500351 (2016).
20. J. Krüger, R. Plass, L. Cevey, M. Piccirelli, M. Grätzel, and U. Bach, "High efficiency solid-state photovoltaic device due to inhibition of interface charge recombination," Appl. Phys. Lett. **79**(13), 2085–2087 (2001).
21. Y. Guo, C. Liu, K. Inoue, K. Harano, H. Tanaka, and E. Nakamura, "Enhancement in the efficiency of an organic–inorganic hybrid solar cell with a doped P3HT hole-transporting layer on a void-free perovskite active layer," J. Mater. Chem. A Mater. Energy Sustain. **2**(34), 13827–13830 (2014).
22. K. Raja, P. S. Ramesh, and D. Geetha, "Synthesis, structural and optical properties of ZnO and Ni-doped ZnO hexagonal nanorods by Co-precipitation method," Spectrochim. Acta A Mol. Biomol. Spectrosc. **120**, 19–24 (2014).
23. J. H. He, C. S. Lao, L. J. Chen, D. Davidovic, and Z. L. Wang, "Large-scale Ni-doped ZnO nanowire arrays and electrical and optical properties," J. Am. Chem. Soc. **127**(47), 16376–16377 (2005).
24. C. Cheng, G. Xu, H. Zhang, and Y. Luo, "Hydrothermal synthesis Ni-doped ZnO nanorods with room-temperature ferromagnetism," Mater. Lett. **62**(10-11), 1617–1620 (2008).
25. J. Zhao, L. Wang, X. Yan, Y. Yang, Y. Lei, J. Zhou, Y. Huang, Y. Gu, and Y. Zhang, "Structure and photocatalytic activity of Ni-doped ZnO nanorods," Mater. Res. Bull. **46**(8), 1207–1210 (2011).
26. A. P. Rambu, L. Ursu, N. Iftimie, V. Nica, M. Dobromir, and F. Iacomi, "Study on Ni-doped ZnO films as gas sensors," Appl. Surf. Sci. **280**, 598–604 (2013).
27. J. Liu, Y. Shirai, X. Yang, Y. Yue, W. Chen, Y. Wu, A. Islam, and L. Han, "High-Quality Mixed-Organic-Cation Perovskites from a Phase-Pure Non-stoichiometric Intermediate $(FAI)_{1-x}$ -PbI_2 for Solar Cells," Adv. Mater. **27**(33), 4918–4923 (2015).
28. M. D. R. Tolosa, L. C. Damonte, H. Brine, H. J. Bolink, and M. A. Hernández-Fenollosa, "Nucleant layer effect on nanocolumnar ZnO films grown by electrodeposition," Nanoscale Res. Lett. **8**(1), 135 (2013).
29. Y.-C. Chao, C.-Y. Chen, C.-A. Lin, Y.-A. Dai, and J.-H. He, "Antireflection effect of ZnO nanorod arrays," J. Mater. Chem. **20**(37), 8134–8138 (2010).
30. Y.-J. Lee, D. S. Ruby, D. W. Peters, B. B. McKenzie, and J. W. P. Hsu, "ZnO nanostructures as efficient antireflection layers in solar cells," Nano Lett. **8**(5), 1501–1505 (2008).
31. L. Wang, D. Zhao, Z. Su, and D. Shen, "Hybrid polymer/ZnO solar cells sensitized by PbS quantum dots," Nanoscale Res. Lett. **7**(1), 106 (2012).
32. S. Husain, F. Rahman, N. Ali, and P. A. Alvi, "Nickel sub-lattice effects on the optical properties of ZnO nanocrystals," J. Optoelectron. Eng. **1**, 28–32 (2013).
33. A. Azam and S. S. Babkair, "Low-temperature growth of well-aligned zinc oxide nanorod arrays on silicon substrate and their photocatalytic application," Int. J. Nanomedicine **9**, 2109–2115 (2014).
34. E. P. da Silva, M. Chaves, G. J. da Silva, L. B. de Arruda, P. N. Lisboa-Filho, S. F. Durrant, and J. R. R. Bortoleto, "Al-doping effect on the surface morphology of ZnO films grown by reactive RF magnetron sputtering," Mater. Sci. Appl. **4**, 761–767 (2013).
35. A. Henni, A. Merrouche, L. Telli, and A. Karar, "Studies on the structural, morphological, optical and electrical properties of Al-doped ZnO nanorods prepared by electrochemical deposition," J. Electroanal. Chem. **763**, 149–154 (2016).
36. K. Tvingstedt, O. Malinkiewicz, A. Baumann, C. Deibel, H. J. Snaith, V. Dyakonov, and H. J. Bolink, "Radiative efficiency of lead iodide based perovskite solar cells," Sci. Rep. **4**, 6071 (2014).
37. J. Kim, G. Kim, T. K. Kim, S. Kwon, H. Back, J. Lee, S. H. Lee, H. Kang, and K. Lee, "Efficient planar-heterojunction perovskite solar cells achieved via interfacial modification of a sol–gel ZnO electron collection layer," J. Mater. Chem. A Mater. Energy Sustain. **2**(41), 17291–17296 (2014).
38. F. Hao, C. C. Stoumpos, D. H. Cao, R. P. H. Chang, and M. G. Kanatzidis, "Lead-free solid-state organic-inorganic halide perovskite solar cells," Nat. Photonics **8**(6), 489–494 (2014).
39. N. De Marco, H. Zhou, Q. Chen, P. Sun, Z. Liu, L. Meng, E.-P. Yao, Y. Liu, A. Schiffer, and Y. Yang, "Guanidinium: a route to enhanced carrier lifetime and open-circuit voltage in hybrid perovskite solar cells," Nano Lett. **16**(2), 1009–1016 (2016).

Optical Materials EXPRESS

1. Introduction

Perovskite solar cells based on hybrid organic–inorganic alkylammonium lead halides as light absorbers have attracted much attention recently because of superb photovoltaic performance, solution process, and low-cost technology. Several intrinsic properties including a wide visible absorption range from 300 to 800 nm, high absorption coefficient, and long exciton diffusion length make perovskite solar cells suitable for harvesting sunlight. The first attempt to use perovskite as a light harvester was implemented in liquid-type dye-sensitized solar cells, leading to low power conversion efficiency (*PCE*) values of 3.1–3.8% [1]. The *PCE* of the perovskite-based devices was significantly enhanced to 9.7% by adopting a solid-state sandwiched architecture with the configuration of FTO/electron transporting layer (ETL)/perovskite/hole transporting layer (HTL)/Au [2]. The perovskite absorber was sandwiched between the ETL and HTL. A hole-transporting material [2,2',7,7'-tetrakis(*N*,*N*-di-*p*-methoxyphenylamine)-9,9'-spirobifluorene] (spiro-MeOTAD) was utilized as the HTL, and titanium dioxide (TiO_2) film was used as the ETL. The *PCE* value was further improved to 15.4% by interdiffusion of spin-coated stacking layers of lead iodide (PbI_2) and methylammonium iodide (MAI) [3], i.e., PbI_2 and MAI layers were prepared by a two-step spin-coating procedure. An alternative method, namely vapor-assisted solution process, was reported as the following procedure: PbI_2 was spin-cast into thin film, followed by dipping in MAI solution to form the final methylammonium lead iodide ($CH_3NH_3PbI_3$ or $MAPbI_3$) perovskite layer [4]. A high *PCE* of 15% was obtained with the configuration of FTO/TiO_2/$MAPbI_3$/spiro-MeOTAD/Au. Most recently, an inspiring *PCE* up to 20.2% has been reported with the configuration of FTO/blocking TiO_2 layer/mesoporous TiO_2 layer/perovskite/poly[bis(4-phenyl)(2,4,6-trimethyl- phenyl)amine] (PTAA)/Au [5], using formamidinium lead iodide mixed with methylammonium lead bromide $(FAPbI_3)_{1-x}(MAPbBr_3)_x$ as the active layer.

In conventional perovskite solar cells, an *n*-type metal oxide film is usually required as the ETL on the transparent conductive electrode, e.g., indium tin oxide (ITO) and fluorine-doped tin oxide (FTO). Besides, this ETL can prevent direct contact between the oxide electrode and perovskite layer. Compact and/or mesoporous TiO_2 are commonly used as the ETL for constructing perovskite solar cells with high efficiency [2,4,5]. However, TiO_2 has a lower electron transport mobility of 20 cm^2/Vs compared to other metal oxides, such as zinc oxide (ZnO) with electron mobility of 230 cm^2/Vs by the Hall effect measurement [6,7]. The low intrinsic electron mobility of TiO_2 may lead to unbalanced charge transport of perovskite solar cells [8]. Moreover, TiO_2 usually requires a high sintering temperature up to 450 °C to obtain a high-quality crystallization that hinders the development of flexible devices on plastic substrates. In contrast, ZnO is also an *n*-type semiconductor; it has higher electron mobility and a wide direct band gap (E_g) of 3.37 eV at 300 K. ZnO has been reported to be suitable for potential use in inorganic light-emitting diodes and solar cells [9,10]. The sintering temperature of ZnO is also lower ~300 °C. Hence, ZnO has been considered as a good candidate to replace TiO_2 for the fabrication of perovskite solar cells. Kelly *et al.* introduced multi-coated layers of ZnO nanoparticles using room-temperature solution processing techniques as the ETL in perovskite solar cells [11]. The device with the configuration of ITO/ZnO/$MAPbI_3$/spiro-MeOTAD/Ag showed a *PCE* of 14.4%. The short-circuit current density (J_{SC}) and *PCE* of the device were both enhanced as a result of the optimized ZnO thickness of 25 nm. Wang *et al.* employed a low-temperature-processed ZnO–tin dioxide (SnO_2) nanocomposite as the electron collection layer for efficient planar perovskite solar cells [12]. The average *PCE* of 14.0% was achieved from the devices with the configuration of ITO/ZnO–SnO_2/$MAPbI_3$/spiro-MeOTAD/Ag, which was higher than the one using pure ZnO nanoparticles (*PCE* = 13.6%). The *PCE* of the optimized device was further improved to 15.2% by introducing a mesoporous alumina (Al_2O_3) layer between the ZnO–SnO_2 nanocomposite and perovskite layer. Li *et al.* reported an aluminum-doped zinc oxide (AZO) film as a highly stable electron collection layer for perovskite solar cells [13].

Optical Materials EXPRESS

An average *PCE* of 11.8% was achieved from the devices with the configuration of AZO/$MAPbI_3$/spiro-MeOTAD/Au. This kind of cell simplified device structure (without using FTO or ITO as electrode) and exhibited good stability in ambient environment compared with those of devices based on intrinsic ZnO.

In addition to nanoparticle-type ZnO, nanorod-type ZnO has also been applied as the ETL to construct perovskite solar cells. Park *et al.* employed non-doped ZnO nanorods with length of 1 μm for the fabrication of perovskite solar cells [14]. The optimized device with the configuration of FTO/ZnO nanorods/$MAPbI_3$/ spiro-MeOTAD/Au showed a *PCE* of 11.13%. Compared to the perfect spectral response of ZnO nanorods, a reference perovskite solar cell based on TiO_2 nanorods with the same length exhibited lower open-circuit voltage (V_{OC}) of 869 mV and *PCE* of 10.02%. Meng *et al.* prepared AZO shells over the surface of ZnO nanorods with length of 450 nm for the application in $MAPbI_3$-based perovskite solar cells [15]. The V_{OC} and *PCE* of the best device with the configuration of FTO/ZnO nanorods/AZO shell/$MAPbI_3$/spiro-MeOTAD/Au reached 0.9 V and 10.7%, respectively, which were higher than those of the ZnO nanorod-based device without AZO shell (V_{OC} = 0.77 V, *PCE* = 8.6%). The band position and electron density in AZO are suggested to be the origin for this positive effect of interfacial modification between ZnO nanorods and the perovskite layer. Mahmood *et al.* employed 1 μm-height ZnO nanorods/TiO_2 core–shell heterostructure as the ETL for superior light-harvesting and hysteresis free mesoscopic perovskite solar cells [16]. Two types of ZnO nanorods with different aspect-ratio (AR) were prepared for comparison. The device with the configuration of FTO/ZnO nanorods/TiO_2 shell/$MAPbI_3$/spiro-MeOTAD/Au showed average *PCE* values of 11.25% and 12.57% for low and high AR ZnO nanorods/TiO_2 shell-based perovskite solar cells. Superior light harvesting capability, larger surface area, prolonged charge-transport pathways, and lower recombination rate are responsible for better photovoltaic properties of the high AR ZnO nanorods/TiO_2 shell-based device. Apart from vertically grown ZnO nanorods, horizontally-arranged ZnO nanorods have also been applied in perovskite solar cells. Mahmood *et al.* demonstrated a double-layered ZnO film composed of nanosheets at the bottom and decorated with horizontal nanorods [17]. This approach yields a maximum *PCE* of 10.35% from the device with the configuration of FTO/compact ZnO layer/double-layered ZnO film + $MAPbI_3$/spiro-MeOTAD/Ag, which they attribute to the morphology and faster electron transport of the double-layered oxide film.

Spiro-MeOTAD is the most widely used HTL in conventional perovskite solar cells due to its hole transporting ability, excellent optical transparency in the visible range, and good thermal stability [2,12,13,15–17]. However, aside from its hole transporting feature, the complex synthesis, high cost, and low charge carrier mobility of spiro-MeOTAD limit its potential for commercialization [18]. Besides, high doses of spiro-MeOTAD accompanying with small amounts of bis(trifluoromethane)sulfonimide lithium salt (Li-TFSI) and 4-*tert*-butylpyridine (TBP) are essentially required to achieve good hole transporting properties for efficient perovskite solar cells. Relative to small-molecule spiro-MeOTAD, poly(3-hexylthiophene-2,5-diyl) (P3HT) is a regioregular semiconducting polymer with high hole mobility up to 0.1 cm^2/Vs and good film-forming property [19]. The price of P3HT is also lower than that of commercial spiro-MeOTAD, which is beneficial for commercialization and mass production. To improve the hole extraction ability, the Li-TFSI salt can be added into P3HT as HTL to increase the carrier density in the HTL and reduce recombination losses in perovskite solar cells [20,21].

As mentioned above, non-doped ZnO nanorods, ZnO nanorods/AZO core-shell, ZnO nanorods/TiO_2 core-shell, multi-layered ZnO nanoparticles, and ZnO-SnO_2 nanocomposites have been reported in the area of perovskite solar cells. However, nickel (Ni)-doped ZnO nanorods have not been applied as ETL for the fabrication of perovskite solar cells so far. The unique chemical stability of Ni on zinc sites recognizes it as one of the most efficient doping elements to improve and tune the optical and electrical properties of ZnO [22]. Chen *et al.* reported large-scale Ni-doped ZnO nanowire arrays with improved electrical conductivity

Optical Materials EXPRESS

compared to the undoped ones [23]. Cheng *et al.* reported Ni-doped ZnO nanorods by the hydrothermal synthesis at a high temperature up to 140 °C to be applied build components in spintronic devices [24]. Zhang *et al.* demonstrated Ni-doped ZnO nanorods with higher photocatalytic activity than the undoped ZnO [25]. Besides, Ni-doped ZnO films were utilized as gas sensors for the detection of ammonia, and they showed higher sensitivity compared with pure ZnO or nickel oxide [26].

Herein, we report on the low-temperature hydrothermal synthesis of non-doped and Ni-doped ZnO nanorods for the fabrication of perovskite solar cells. The lengths of nanorods are reduced to 300 nm to increase transmittance of ZnO in the visible region, which is beneficial for incident photons to enter devices and to be absorbed by the active layer. Novel perovskite solar cells with the configuration of ITO/Ni-doped ZnO nanorods/ [6,6]-phenyl-C_{61}-butyric acid methyl ester (PCBM)/perovskite/P3HT + Li-TFSI/Au were fabricated and evaluated. In addition to $MAPbI_3$, two different kinds of perovskite materials, including methylammonium/formamidinium lead iodide $(MA)_x(FA)_{1-x}PbI_3$ and methylammonium/guanidinium lead iodide $(MA)_y(GA)_{1-y}PbI_3$ were utilized as the light harvesters. Our results revealed a maximum *PCE* of 13.79% with the device using Ni-doped ZnO nanorods as ETL and $(MA)_y(GA)_{1-y}PbI_3$ as the active layer. Miscellaneous characterization techniques, including scanning electron microscopy (SEM), atomic force microscopy (AFM), X-ray diffraction (XRD) analysis, and optical measurements were also performed and demonstrated in this work.

2. Experimental

2.1 Materials

All chemicals were purchased from Alfa Aesar, Sigma-Aldrich or Acros and used without further purification. All solutions were filtered with 0.45 μm polytetrafluoroethylene (PTFE) filters before use. Methylammonium iodide (MAI) was synthesized by reacting methylamine and hydroiodic acid together for 4 hr, and the crude product was collected and purified by re-precipitation in diethyl ether for several times. The overall yield of MAI is 65%. Formamidinium Iodide (FAI) was synthesized by reacting formamidinium acetate and hydroiodic acid together for 4 hr, and the crude product was collected and purified by re-precipitation in diethyl ether for several times [27]. Guanidinium Iodide (GAI) was purchased from Sigma-Aldrich.

2.2 Preparation of ZnO nanorod arrays

The non-doped and Ni-doped ZnO nanorod arrays were prepared by the hydrothermal method on the ITO substrates. The ITO/glass substrates (7 Ω/sq) were cleaned with detergent, acetone, and isopropyl alcohol (IPA) under ultrasonication, followed by nitrogen purge and drying in an oven. The preparation of ZnO nanorod arrays on the ITO substrates is shown in Fig. 1. The detailed fabrication process is described as follows. A solution of zinc acetate dihydrate (0.5487 g, 2.5 mmol) in 10 mL of IPA was stirred vigorously at 60 °C for 5 min. 2-(Dimethylamino)ethanol (0.2228 g, 2.5 mmol) was slowly added to the above solution and stirred at the same temperature for an additional 2 hr to form a homogeneous precursor solution. This precursor solution was then spin-cast into thin film at 3,000 rpm for 30 s and calcinated at 200 °C in air for 30 min to form ZnO seed layers with thickness of 50 nm.

The next step is to prepare non-doped and Ni-doped ZnO nanorods on the seed layers. A solution consisting of zinc sulfate heptahydrate (0.287 g, 1 mmol) and ammonium chloride (2.14 g, 40 mmol) in 150 mL of de-ionized water was prepared. For Ni-doping, two different amounts of nickel(II) acetate hydrate (0.0025 g or 0.005 g) were added into the above zinc sulfate solution. The Ni doped proportion is labelled as 1% or 2%, respectively, equal to Ni / (Ni + Zn) (mol%). 2M NaOH aqueous solution was then slowly added into three separate solutions to adjust their *p*H values to 10.7 to form the bath solution. The ZnO seed layers on

Optical Materials EXPRESS

the ITO substrates were immersed in the above bath solution (ZnO seed layers downward) and placed in a preheated oven (65 °C) for 45 min. The substrates were then washed with de-ionized water and IPA for 10 minutes to remove the residues, followed by calcinations at 300 °C in air for 30 min to form non-doped and Ni-doped ZnO nanorod arrays. The heights of those ZnO nanorods were estimated to be 300 nm by SEM cross-sectional observation.

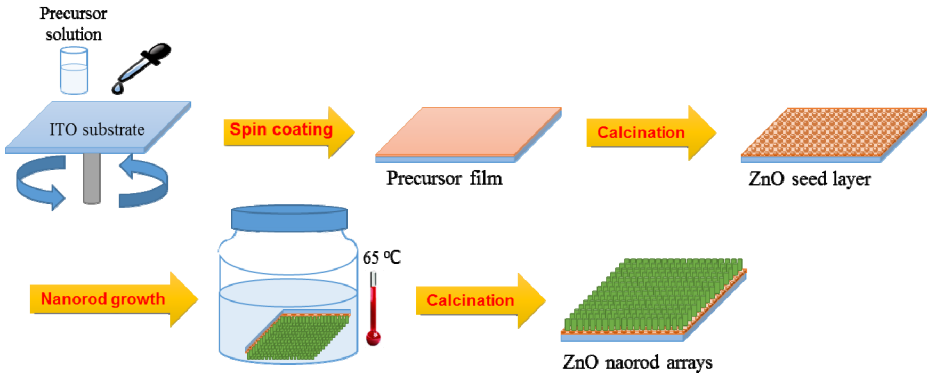

Fig. 1. Schematic illustration of fabrication process of the ZnO nanorod arrays on the ITO substrate.

2.3 Fabrication of perovskite solar cells

The fabrication process of perovskite solar cells based on ZnO nanorod arrays is illustrated in Fig. 2. The devices with the configuration of ITO/non-doped or Ni-doped ZnO nanorods/PCBM/perovskite/P3HT + Li-TFSI/Au were fabricated. The selection of the perovskite includes $MAPbI_3$, $(MA)_x(FA)_{1-x}PbI_3$, and $(MA)_y(GA)_{1-y}PbI_3$, which were prepared by the two-step coating process. A PCBM solution in chlorobenzene (10 mg/mL) was spin-coated onto the ZnO nanorod arrays at 3,000 rpm for 30 s and annealed at 100 °C for 5 min. First, a PbI_2 solution in *N,N*-dimethylformamide (450 mg/mL) was spin-coated onto ZnO nanorod arrays at 5,500 rpm for 30 s and annealed at 100 °C in a vacuum oven for 30 min. Second, three different solutions, namely MAI (40 mg/mL in IPA), MAI + FAI (12:1 in molar ratio), and MAI + GAI (6:1 in molar ratio), were loaded on PbI_2 layer for 60 s and then spin-coated at 5,500 rpm for 30 s separately, followed by annealing at 100 °C in a vacuum oven for 30 min. A P3HT solution in chlorobenzene (20 mg/mL) was added to a lithium salt solution (0.54 mg of Li-TFSI in 6.8 µL of acetonitrile) and spin-coated on the perovskite layer at 1,000 rpm for 30 s, followed by annealing in a vacuum oven at 95 °C for 30 min. Finally, 80 nm-thick Au electrodes were deposited onto P3HT layer by thermal evaporation at base pressure of 10^{-6} torr. The active area of devices is 1 mm^2. The thickness of each layer is estimated from the cross-section SEM image (see the Appendix, Fig. 10). It is also found that PCBM is filled in the bottom of the ZnO nanorod arrays, as verified the SEM observation (see the Appendix, Fig. 11).

Optical Materials EXPRESS

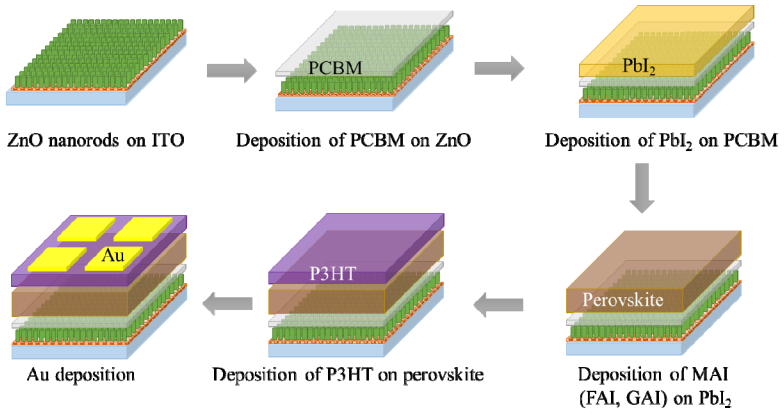

Fig. 2. Fabrication procedure of perovskite solar cells based on the ZnO nanorod arrays.

2.4 Characterization methods

The current density-voltage (J-V) characteristics of photovoltaic devices were taken using a Keithley 2400 source measurement unit under a simulated AM 1.5G exposure with a 1000 W Xenon Short Arc Lamp (USHIO UXL-10S). The simulated solar source was calibrated with a commercial silicon reference cell. The UV-vis absorption spectra of films were acquired at room temperature by a Princeton Instruments Acton 2150 spectrophotometer with a 150 W Xenon lamp (USHIO UXL-150S). Steady-state PL spectra were measured using a fluorescent spectrophotometer (Princeton Instruments Acton 2150) equipped with a 30 mW KIMMON KOHA He-Cd laser (325/442 nm) as excitation sources. For UV-Vis transmission and absorption measurements using a Xe lamp as the light source, the optical spot size is 3 × 3 mm^2 and the direction of the unpolarized incident light is perpendicular ($\theta = 90°$) to the sample surface. For PL measurements using a He-Cd laser as the light source, the beam diameter is 0.94 mm and the direction of the linear polarized incident light is 30° to the normal direction of the sample surface. The surface morphology of films was measured by a Bruker Innova atomic force microscopy (AFM) instrument. Top-view and cross-section scanning electron microscopy (SEM) observations were performed with a JEOL JSM-6700F SEM instrument. The transmission electron spectroscopy (TEM) and high resolution TEM (HRTEM) were performed with a JEOL JEM-2010 TEM instrument. X-ray diffraction (XRD) patterns were obtained from a Rigaku D/MAX 2500 X-ray diffractometer. The Hall measurement was carried out with a BioRad HL5500 Hall Effect Measurement System. The external quantum efficiency (EQE) measurement was conducted using a PV Measurements QEX10 instrument.

3. Results and discussions

3.1 Characterization of ZnO nanorod arrays

The side-view and top-view SEM micrographs of non-doped and Ni-doped ZnO nanorod arrays are shown in Fig. 3. It is seen that growth direction of ZnO nanorods is mainly vertical to the ITO substrate. The lengths of ZnO nanorods are estimated to be 280–300 nm from side-view SEM, and the diameters of ZnO nanorods are in the range of 35–60 nm from top-view SEM. Besides, there are still some spaces for perovskite materials to fill in. The AFM topographic and 3D images of ZnO nanorod arrays are shown in Fig. 4. It is clearly seen that the morphology of ZnO nanorods are consistent with SEM observation. The surface roughness (R_a) values of non-doped, 1% Ni-doped, and 2% Ni-doped ZnO nanorod arrays are calculated to be 26.6 nm, 18.4 nm, and 19.2 nm, respectively. The SEM and AFM observations of our non-doped ZnO nanorods arrays are similar to the previous reports [14,28]. In addition, we notice that Ni-doped ZnO nanorods possess more aligned

Optical Materials EXPRESS

morphologies and smaller R_a value compared with the non-doped ones, implying better transporting property for carriers. The TEM and HRTEM images of Ni-doped ZnO nanorods are shown in the supplementary information (see Fig. 12). The diameter and shape of a single ZnO nanorod are clearly observed.

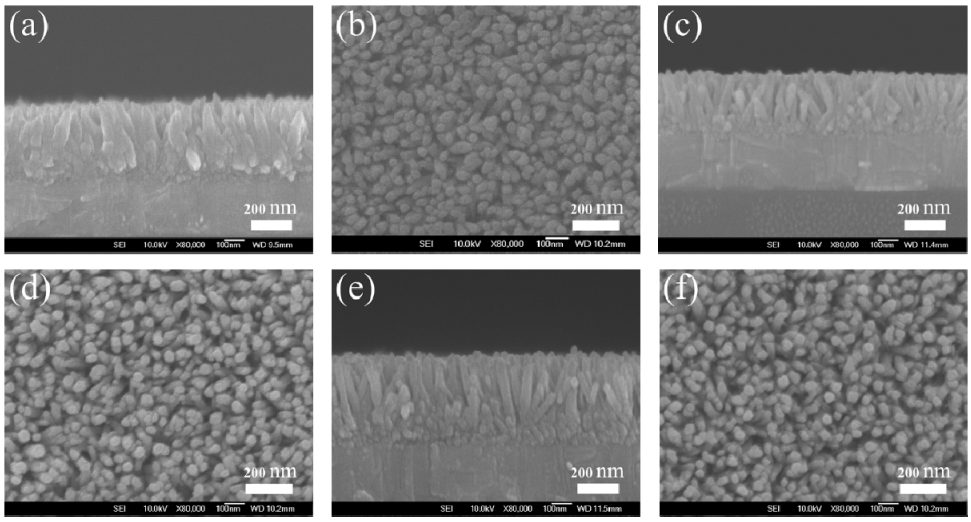

Fig. 3. Side-view and top-view SEM micrographs of (a) (b) non-doped, (c) (d) 1% Ni-doped, and (e) (f) 2% Ni-doped ZnO nanorods arrays.

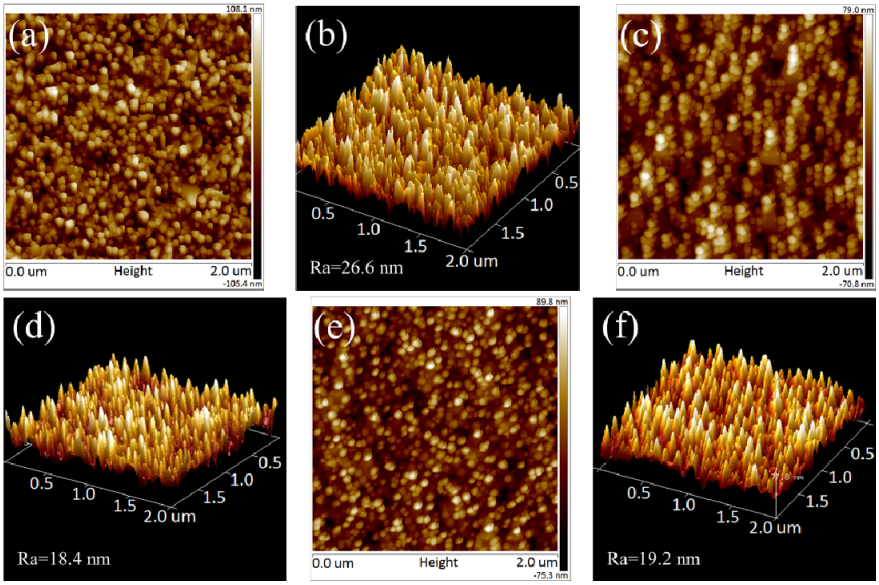

Fig. 4. AFM topographic and 3D images of (a) (b) non-doped, (c) (d) 1% Ni-doped, and (e) (f) 2% Ni-doped ZnO nanorod arrays.

The UV–vis transmission and absorption spectra of non-doped and Ni-doped ZnO nanorods and ITO substrate are shown in Fig. 5(a) and 5(b), respectively. The transmittance of ZnO nanorod arrays is sufficiently high up to 90% in the visible range. Moreover, ZnO nanorods on the ITO reveal even higher transmittance than the bare ITO substrate. The reason to this phenomenon can be explained by the anti-reflection effect of ZnO, which has been reported in the previous literature [29,30]. From Fig. 5(b) the absorption bands of non-doped

Optical Materials EXPRESS

and Ni-doped ZnO nanorods are located in the range of 250–380 nm that are in accordance with the previous report [31]. Besides, it is noted that Ni-doped ZnO nanorods possess slightly higher absorption around 360 nm, which is attributed to NiO formation in ZnO nanorods, i.e., Ni-doping process [32]. The absorption edges of both non-doped and Ni-doped ZnO nanorods are found at 380 nm, corresponding to their optical bandgaps of 3.26 eV. We conclude that the optical bandgap of ZnO nanorods was not affected by Ni-doping.

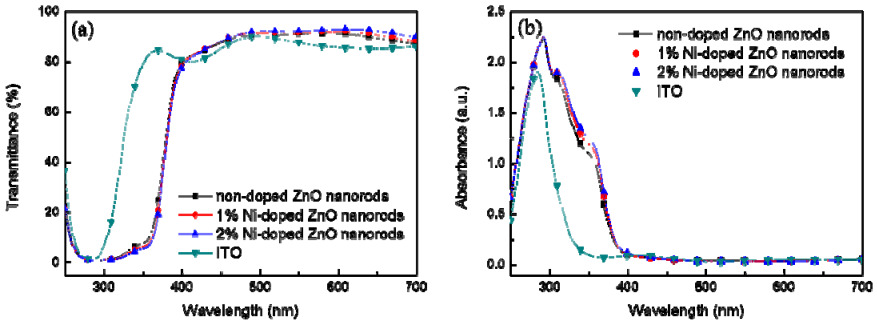

Fig. 5. (a) Transmission and (b) absorption spectra of bare ITO, non-doped, 1%, and 2% Ni-doped ZnO nanorods.

Figure 6 shows the XRD patterns of the prepared ZnO nanorod arrays. The diffraction peaks of the ZnO nanorods are well matched with the ZnO standard (JCPDS 36-1451, see the Appendix, Fig. 13) [33]. The highly oriented nature of our ZnO nanorods is connected with the intense diffraction peak at $2\theta = 34.4°$ along (002) reflection [33,34]. The sharp and strong (002) reflection also indicates preferred crystallization of ZnO nanorods along the *c*-axis direction, i.e., vertical to the substrate surface. Moreover, the incorporation of Ni atoms can be deduced from two increased peaks indexed (100) and (101) compared to the strong (002) peak, which is due to the formation of stress-induced ion size difference between Zn and Ni and the segregation of Ni in grain boundaries [35]. The incorporation of Ni ions into the Zn site of the ZnO matrix is also verified by the energy dispersive X-ray (EDX) spectra (see the Appendix, Fig. 14). The presence of Zn, O, and Ni clearly indicates successful preparation of Ni-doped ZnO samples in this study.

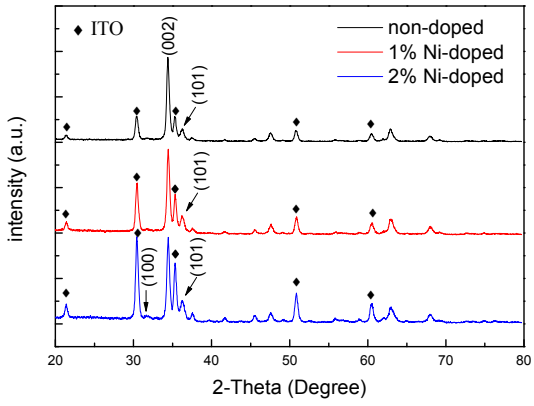

Fig. 6. XRD patterns of non-doped and Ni-doped ZnO nanorod arrays.

Optical Materials EXPRESS

To further compare the conductivity of non-doped and Ni-doped ZnO nanorod arrays, simple sandwiched devices with the configuration of ITO/ZnO/Au were fabricated and their current-voltage characteristics were measured (see the Appendix, Fig. 15). It is observed that the device based on the 2% Ni-doped ZnO nanorod arrays show the highest electrical conductivity and lowest resistance among three samples, indicative of higher electron transporting properties for photovoltaic devices. The Hall measurement of non-doped and Ni-doped ZnO nanorod arrays was also performed (see the Appendix, Fig. 16). It reveals that higher mobility of ZnO is obtained as the doping concentration of Ni is increased.

3.2 Characterization of perovskite films on ZnO nanorod arrays

The top-view SEM images of perovskite $MAPbI_3$, $(MA)_x(FA)_{1-x}PbI_3$, and $(MA)_y(GA)_{1-y}PbI_3$ films are displayed in Fig. 7(a)–7(c), respectively, indicative of homogeneous distribution of perovskite grains with sizes of 300–700 nm on non-doped ZnO nanorods. There are still small pinholes to be observed for $MAPbI_3$ and $(MA)_x(FA)_{1-x}PbI_3$ on ZnO nanorods from SEM micrographs, which might affect the fill factor (*FF*) and performance of photovoltaic devices. Compared to the similar report of the perovskite film on 1000 nm-height ZnO nanorods, pinholes in this study were significantly reduced and the coverage ratio of the perovskite film was improved [14]. Besides, those pinholes can be filled by depositing the next P3HT layer, preventing direct contact between top gold electrode and ZnO nanorods. It is noteworthy that the $(MA)_y(GA)_{1-y}PbI_3$ represents a compact and pinhole-free film on ZnO nanorods among three perovskite films. The surface morphologies of perovskite films are observed from topographic AFM image in Fig. 7(d)–7(f). The grain distribution of these perovskite crystals from AFM is consistent with the SEM observation. The R_a values of $MAPbI_3$, $(MA)_x(FA)_{1-x}PbI_3$, and $(MA)_y(GA)_{1-y}PbI_3$ films on ZnO nanorods were measured to be 14.1, 15.1, and 18.7 nm, respectively. The steady-state PL spectra of the perovskite $MAPbI_3$ on the bare glass, non-doped, and Ni-doped ZnO nanorods are shown in Fig. 8. The max PL emission of the perovskite is located at 770 nm under excitation of a He-Cd laser source, which is in accordance with the previous literature [13]. The significant PL quenching of the perovskite is found when depositing on non-doped ZnO nanorods, implying charge extraction across the interface between the perovskite and ZnO [36]. By depositing perovskite on Ni-doped ZnO nanorods, the PL emission of the perovskite is further prohibited, indicative of more effective carrier extraction and reduced recombination, which will help to improve J_{SC} and performance of perovskite solar cells. It is known that the grain size of the perovskite could make an important attribution to PL spectra and thus the device performance. Hence, the AFM investigation of $MAPbI_3$ on bare glass, non-doped, and 2% Ni-doped ZnO nanorods was carried out. (see the Appendix, Fig. 17). It is seen that that the grain sizes of three perovskite samples are similar. Hence, the size effect for PL quenching experiments in Fig. 8 as well as device performance can be excluded.

Optical Materials EXPRESS

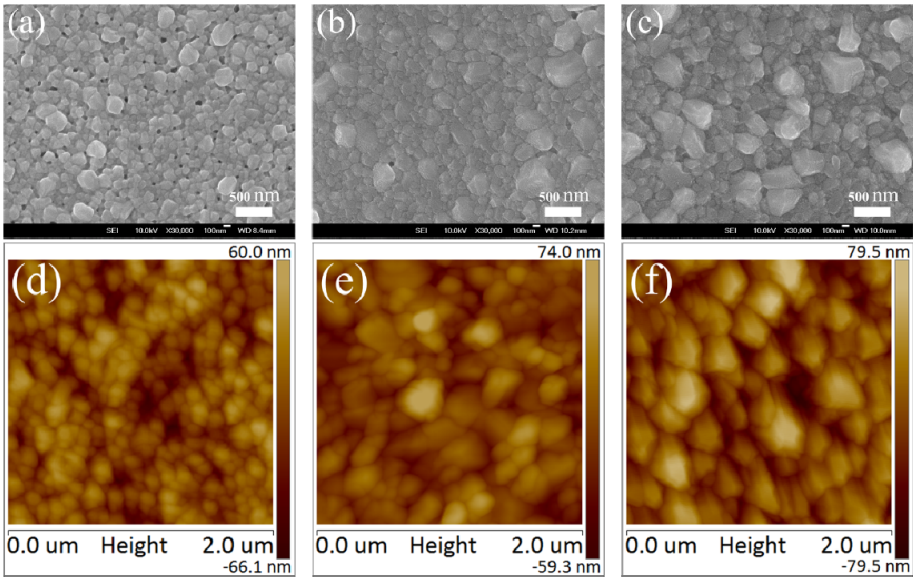

Fig. 7. (a)–(c) SEM and (d)–(f) AFM topographic images of $MAPbI_3$, $(MA)_x(FA)_{1-x}PbI_3$, and $(MA)_y(GA)_{1-y}PbI_3$ films on non-doped ZnO nanorods, respectively.

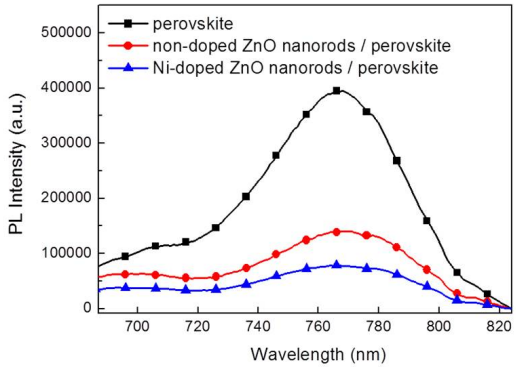

Fig. 8. Steady-state PL spectra of perovskite films on bare glass, non-doped, and Ni-doped ZnO nanorods.

3.3 Device fabrication and evaluation

The J-V characteristics of the solar cells using non-doped and Ni-doped ZnO nanorods as the ETL are shown in Fig. 9(a). The optimized perovskite solar cell based on non-doped ZnO nanorods demonstrated a J_{SC} of 21.33 mA/cm^2, a V_{OC} of 0.81 V, a *FF* of 0.6 and a *PCE* of 10.37% under the AM 1.5G illumination. A similar perovskite solar cell based on non-doped ZnO nanorods with length of 1 μm was reported by Park *et al.* [14], revealing J_{SC}, V_{OC}, *FF*, and *PCE* values of 20.08 mA/cm^2, 0.99 V, 0.56, and 11.13%, respectively. It is seen that the performance of our devices is comparable with the previous result in the literature. By using 1% Ni-doped ZnO nanorods as the ETL, the device parameters J_{SC}, *FF*, and *PCE* were improved to 22.46 mA/cm^2, 0.67, and 12.19%, respectively, while the V_{OC} remained unchanged. By using 2% Ni-doped ZnO nanorods as the ETL, the optimized perovskite solar cell achieved a J_{SC} of 23.18 mA/cm^2, a V_{OC} of 0.81 V, a *FF* of 0.68 and a *PCE* of 12.77% under the same illumination. The device parameters of perovskite solar cells based on non-doped and Ni-doped ZnO nanorods are summarized in Table 1. We conclude that the V_{OC} of devices was not affected by Ni-doping process. The significant increase in J_{SC} and *FF* can be

Optical Materials EXPRESS

explained by better extraction of electrons and reduced series resistance (R_s) for the devices based on Ni-doped ZnO nanorods. As mentioned previously, more effective carrier extraction between the perovskite and Ni-doped ZnO nanorods has been verified by PL quenching experiments. The R_s values can be estimated from the slope of the J-V characteristics at the V_{OC} point that is commonly employed in the previous literature [37,38]. The R_s value of the device using non-doped ZnO nanorods as the ETL was calculated to be 5.91 ohms-cm^2, and it was reduced to 4.69 and 3.47 ohms-cm^2 for the devices using 1% and 2% Ni-doped ZnO nanorods as the ETL. Previous works have been focused on the modification of ZnO nanorods by covering with other materials such as TiO_2 and AZO to form core-shell heterojunctions [15,16]. In this research, we demonstrate Ni-doped ZnO nanorods as ETL that has not been reported in the development of perovskite solar cells so far.

To further improve the efficiency of Ni-doped ZnO nanorods-based perovskite solar cells, two different kinds of perovskite materials, including $(MA)_x(FA)_{1-x}PbI_3$ and $(MA)_y(GA)_{1-y}PbI_3$, were utilized as the active layers. It is reported that high-quality mixed-organic-cation perovskite $(MA)_x(FA)_{1-x}PbI_3$ exhibits photovoltaic performance superior to that of $MAPbI_3$ owing to the broader light-harvesting spectrum and the collection of longer-wavelength photons [27]. Another perovskite material $(MA)_y(GA)_{1-y}PbI_3$ also possesses better device performance compared with $MAPbI_3$, which is due to significantly enhanced carrier lifetimes and V_{OC} [39]. In this study, a mixture of MAI and FAI (or GAI) with molar ratio of 12:1 (or 6:1) were prepared, and perovskite layers were obtained by the same two-step coating process. Besides, the 2% Ni-doped ZnO nanorod arrays were selected as the ETL for the fabrication of perovskite solar cells, since they demonstrated better photovoltaic properties compared with non-doped or 1% Ni-doped ones. The J-V curves of perovskite solar cells using $MAPbI_3$, $(MA)_x(FA)_{1-x}PbI_3$, and $(MA)_y(GA)_{1-y}PbI_3$ as light absorbers are depicted in Fig. 9(b). The optimized device based on $(MA)_x(FA)_{1-x}PbI_3$ produced a J_{SC} of 23.88 mA/cm^2, a V_{OC} of 0.82 V, and a *FF* of 0.64, yielding a *PCE* of 12.53%. By replacing with $(MA)_y(GA)_{1-y}PbI_3$ as the active layer, the optimized device showed even higher photovoltaic performance, including a J_{SC} of 23.73 mA/cm^2, a V_{OC} of 0.83 V, a *FF* of 0.7, and a *PCE* of 13.79%. The device parameters of perovskite solar cells using different perovskite layers on the 2% Ni-doped ZnO nanorods are summarized in Table 2. It is concluded that the perovskite solar cell composed of $(MA)_y(GA)_{1-y}PbI_3$ and the 2% Ni-doped ZnO nanorod arrays reveals the highest efficiency in this research. The EQE spectra of the devices based on $MAPbI_3$, $(MA)_x(FA)_{1-x}PbI_3$, and $(MA)_y(GA)_{1-y}PbI_3$ on the 2% Ni-doped ZnO nanorod arrays are shown in Fig. 9(c), which is similar to the previous work using ZnO film as ETL [37]. The $(MA)_y(GA)_{1-y}PbI_3$ device revealed the highest EQE values among three devices, with the EQE maximum approaching 80% around 500 nm. The EQE of the $(MA)_x(FA)_{1-x}PbI_3$ device was higher than that of the $MAPbI_3$ one in the range of 600–800 nm due to better conversion of long-wavelength photons [27]. The EQE trend of the three devices is in good accordance with their photovoltaic performance, as revealed in Fig. 9(b) and Table 2.

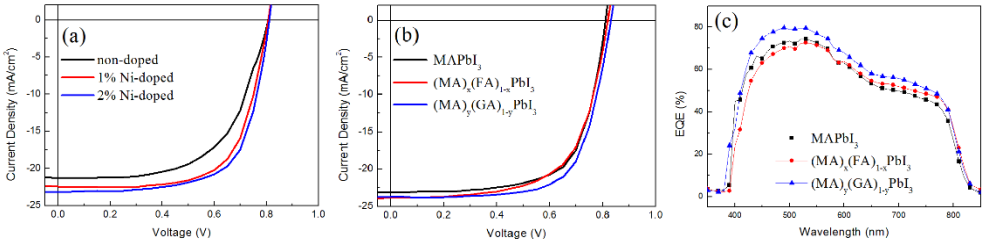

Fig. 9. (a) J-V characteristics of $MAPbI_3$ on non-doped and Ni-doped ZnO nanorods; (b) J-V characteristics and (c) EQE spectra of different perovskite solar cells based on 2% Ni-doped ZnO nanorods.

Optical Materials EXPRESS

Table 1. Performance of perovskite solar cells based on non-doped and Ni-doped ZnO nanorods.

ZnO	V_{OC} (V)	J_{SC} (mA/cm^2)	*FF*	*PCE* (%)	Avg. *PCE*[a] (%)	R_s[b] (ohms-cm^2)
non-doped	0.81	21.33	0.6	10.37	9.58	5.91
1% Ni-doped	0.81	22.46	0.67	12.19	11.68	4.69
2% Ni-doped	0.81	23.18	0.68	12.77	12.03	3.47

[a] Average *PCE* values were obtained from 18 devices.
[b] The R_s of the perovskite solar cells was calculated using $(dJ/dV)^{-1}$ at $V = V_{OC}$.

Table 2. Performance of perovskite solar cells using different perovskite layers on Ni-doped ZnO nanorods.

perovskite	V_{OC} (V)	J_{SC} (mA/cm^2)	*FF*	*PCE* (%)	Avg. *PCE*[a] (%)
$MAPbI_3$	0.81	23.18	0.68	12.77	12.03%
$(MA)_x(FA)_{1-x}PbI_3$	0.82	23.88	0.64	12.53	11.46%
$(MA)_y(GA)_{1-y}PbI_3$	0.83	23.73	0.7	13.79	12.88%

[a] Average *PCE* values were obtained data from 18 devices.

4. Conclusion

Ni-doped ZnO nanorod arrays with well-aligned morphologies were successfully prepared via the hydrothermal method. The transmittance of Ni-doped ZnO nanorods is sufficiently high up to 90% in the visible range, and the presence of Ni ions is confirmed by UV-vis absorption, XRD, and EDX experiments. The quenching of PL emission of the perovskite on Ni-doped ZnO nanorods indicates effective carrier extraction and reduced recombination, which is favored for carrier transfer from perovskite to ZnO. Pinhole-free $(MA)_y(GA)_{1-y}PbI_3$ film with larger grain size was obtained on ZnO nanorods. The best device with a *PCE* of 13.79% was achieved using the 2% Ni-doped ZnO nanorod arrays as the ETL and $(MA)_y(GA)_{1-y}PbI_3$ as the active layer.

Appendix

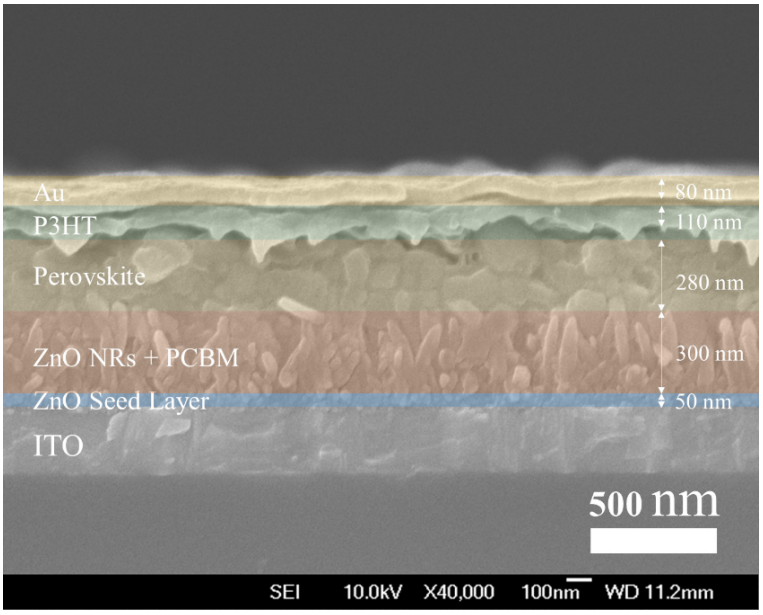

Fig. 10. Cross-section SEM image of the best device based on $(MA)_y(GA)_{1-y}PbI_3$ on 2% Ni-doped ZnO nanorod arrays.

Optical Materials EXPRESS

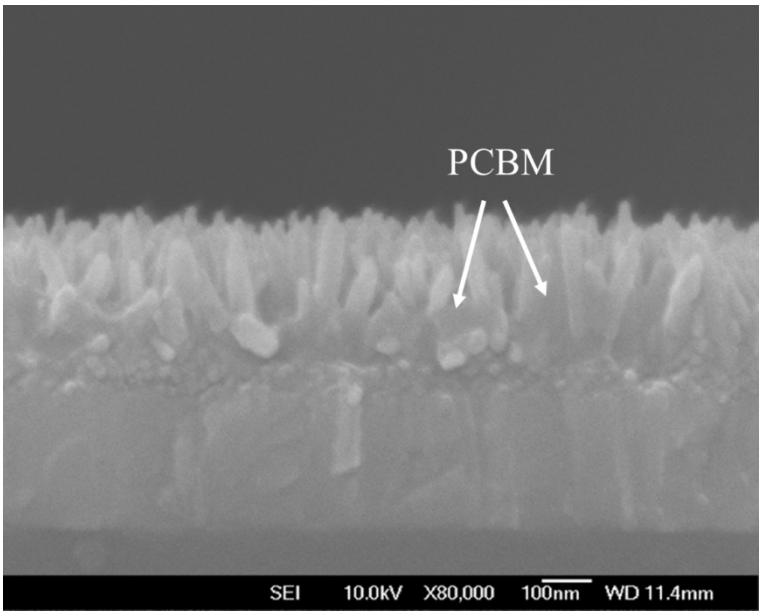

Fig. 11. Cross-section SEM image of PCBM/ZnO nanorod arrays.

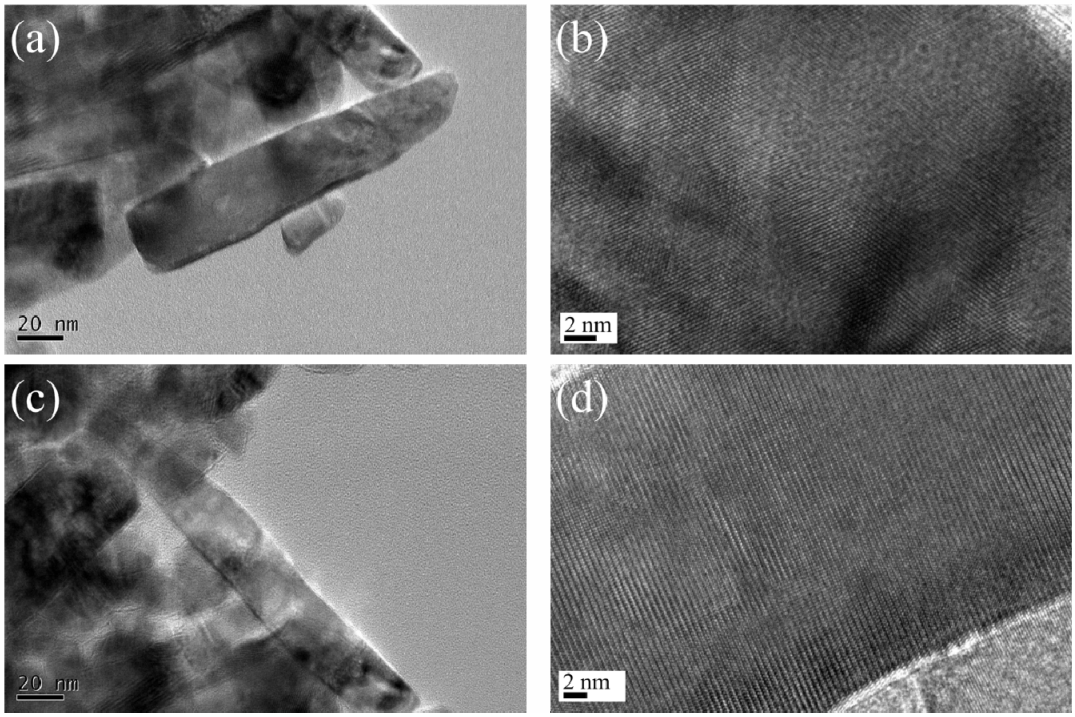

Fig. 12. TEM and HRTEM images of (a) (b) 1% Ni-doped and (c) (d) 2% Ni-doped ZnO nanorods.

Optical Materials EXPRESS

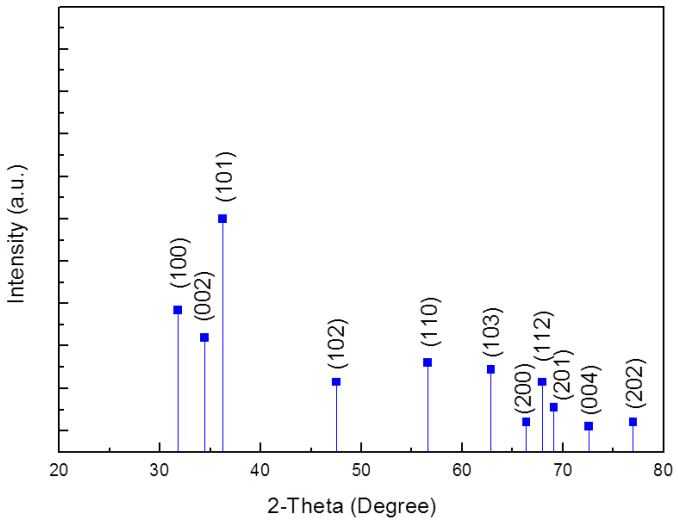

Fig. 13. ZnO standard (JCPDS 36-1451).

Optical Materials EXPRESS

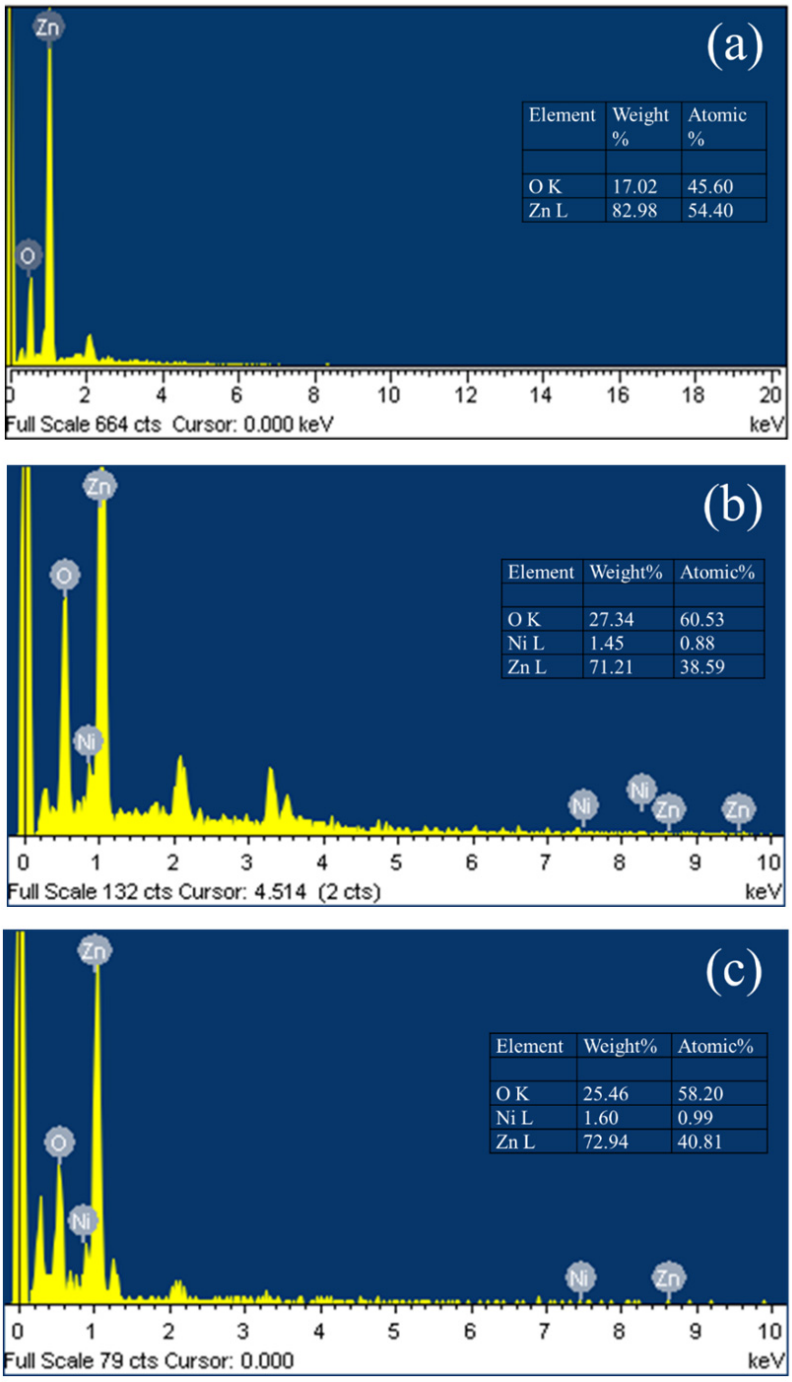

Fig. 14. EDX spectra of (a) non-doped, (b) 1% Ni-doped, and (c) 2% Ni-doped ZnO nanorods.

Optical Materials EXPRESS

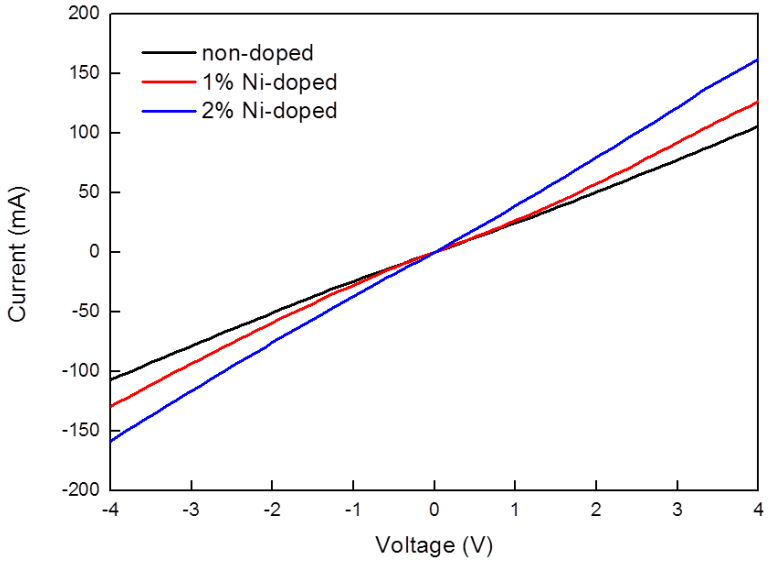

Fig. 15. I-V characteristics of devices based on non-doped, 1% Ni-doped, and 2% Ni-doped ZnO nanorods. The device structure is ITO/ZnO/Au.

Optical Materials EXPRESS

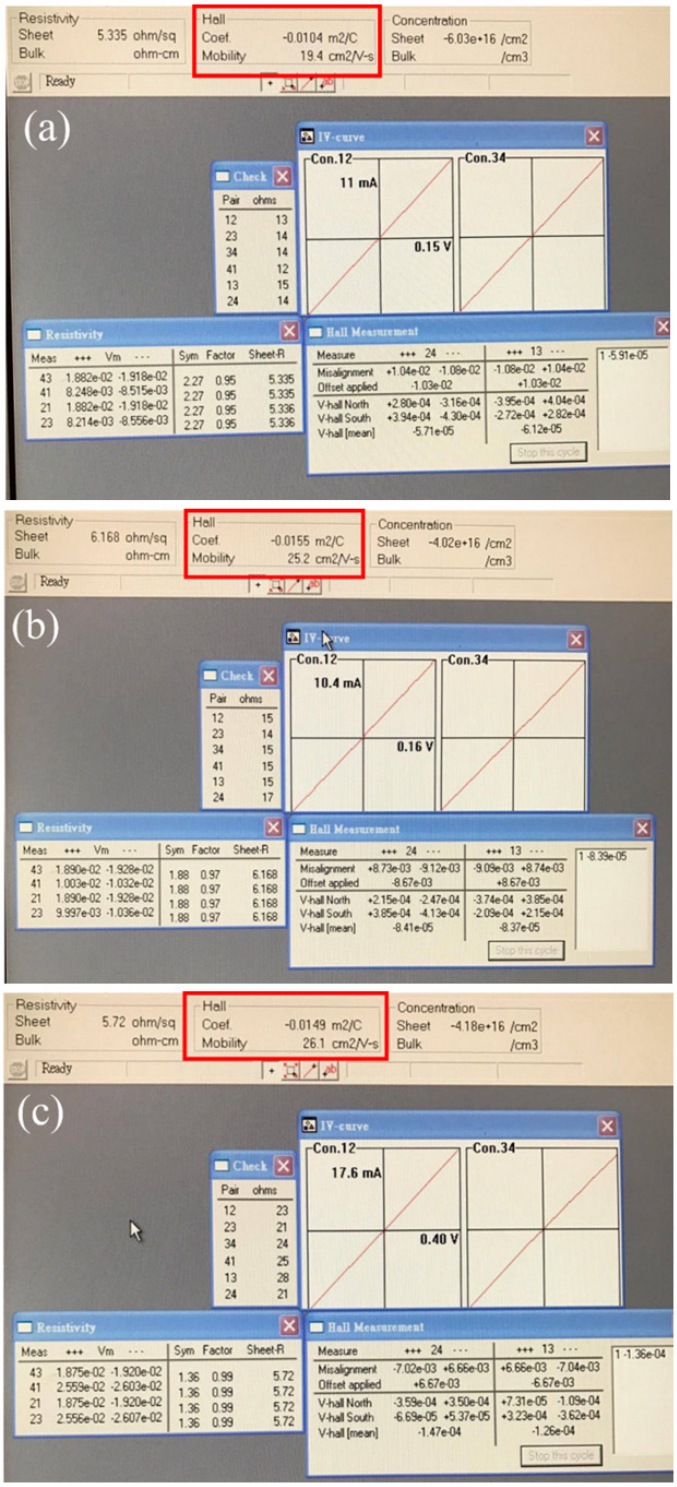

Fig. 16. Screen pages of mobility data of (a) non-doped, (b) 1% Ni-doped, and (c) 2% Ni-doped ZnO nanorod arrays by the Hall measurement.

Optical Materials EXPRESS

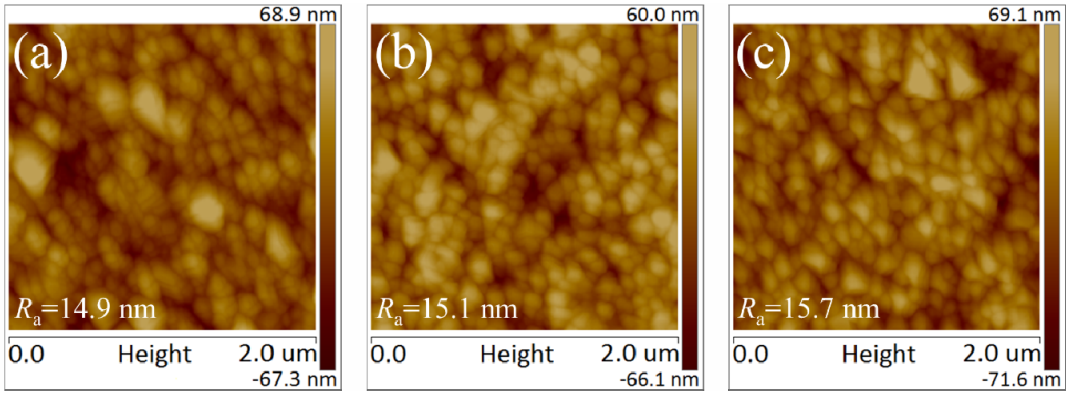

Fig. 17. AFM topographic images of $MAPbI_3$ on (a) bar glass, (b) non-doped, and (c) 2% Ni-doped ZnO nanorods.

Funding

Ministry of Science and Technology of Republic of China (MOST 104-2221-E-009-187).

Acknowledgments

The authors thank the Ministry of Science and Technology of Republic of China for financial support of this work. The authors also thank Dr. Kun-Lin Lin from the National Nano Device Laboratories for his kind help in TEM and HRTEM investigations.